Variation of the subsidence parameters, effective thermal conductivity, and mantle dynamics

Adam C., S. D. King, V. Vidal, M. Rabinowicz, A. Jalobeanu, and M. Yoshida

Abstract

The subsidence of seafloor is generally considered to be a passive phenomenon related to the conductive cooling of the lithosphere after its creation at mid-oceanic ridges. Recent alternative theories suggest that the mantle dynamics plays an important role in the structure and depth of the oceanic lithosphere. However, the link between mantle dynamics and seafloor subsidence has still to be quantitatively assessed. Here we provide a statistical study of the subsidence parameters (subsidence rate and ridge depth) for all the oceans. These parameters are retrieved through two independent methods, the positive outliers method, a classical method used in signal processing, and through the MiFil method. From the subsidence rate, we compute the effective thermal conductivity, k_{eff}. This parameter ranges between 1 and 7 Wm^{-1}K^{-1}. We also model the mantle flow pattern from the S40RTS tomography model. The density anomalies derived from S40RTS are used to compute the instantaneous flow in a global 3D spherical geometry. We show that departures from the k_{eff}=3 Wm^{-1}K^{-1} standard value are systematically related to mantle processes and not to lithospheric structure. Regions characterized by k_{eff}>3 Wm^{-1}K^{-1} are associated with mantle uplifts (mantle plumes or other local anomalies). Regions characterized by k_{eff}<3 Wm^{-1}K^{-1} are related to large scale mantle downwellings such as the Australia-Antarctic Discordance (ADD) or the return flow from the South Pacific Superswell to the East Pacific Rise. This demonstrates that the mantle dynamics plays a major role in the shaping of the oceanic seafloor. In particular, the parameters generally considered to quantify the lithosphere structure, such as the thermal conductivity, are not only representative of this structure but also incorporate signals from the mantle convection occurring beneath the lithosphere. The dynamic topography computed from the S40RTS tomography model reproduces the subsidence pattern observed in the bathymetry. Overall we find a good correlation between the subsidence parameters derived from the bathymetry and the dynamic topography. This demonstrates that these parameters are strongly dependent on mantle dynamics.

1. Introduction

Mid-oceanic ridges are divergent margins where lithospheric plates are formed, as hot material rises and then cools as it moves away. As the lithosphere cools its density increases and the seafloor deepens. In classical thermal models, the subsidence rate is defined as the deepening of the seafloor as a function of the square root of its age. The subsidence parameters show great variations. The depth of the ridge, Z_R, varies from 1500 to 4000 m (Marty and Cazenave, 1989; Calcagno and Cazenave, 1994; Kane and Hayes, 1994a,b; Perrot at al., 1998) and the subsidence rate, τ, can be as high as 700

m.Myr$^{-1/2}$ and as low as a few tens of m.Myr$^{-1/2}$ (Perrot et al., 1998). Several models have been examined in order to understand the phenomenon controlling the evolution of the subsidence parameters. However, Kane & Hayes' review of the existing thermal models leads to the conclusion that they "cannot account for the large magnitude for subsidence rates (...) and the asymmetry in subsidence rates" (Kane and Hayes, 1994a). Indeed, the temperature variations required to explain the observations are unrealistic, in excess of 1000ºC. A realistic temperature range has been found through a complex geochemical model which links the global correlation of major element chemistry and the ridge depth (Klein and Langmuir, 1987; Kane and Hayes, 1994a). This model, however, has been recently questioned by Niu and O'Hara (2008), who argue that the petrological parameters used as indicators of the extent and pressure of mantle melting beneath mid-oceanic ridges (Na2O and FeO) are unreliable. The most recent models investigate the contributions of temperature-pressure-dependent thermal properties (such as basal temperature, asymptotical plate's thickness, thermal expansivity), axial hydrothermal circulation, and oceanic crust (Hillier and Watts, 2005; Grose and Afonso, 2013). Although some of these variations indirectly take into account the variations of the mantle properties, none of the previous studies has directly considered the dynamics of the mantle. That is the focus of the present study.

In the first part of this work we conduct a statistical study of the seafloor subsidence parameters, using the latest and more accurate data sets. In the second part, we model the instantaneous flow in a global 3D spherical shell geometry, based on the S40RTS tomography model (Ritsema et al., 2010). We then compare these subsidence parameters and the effective thermal conductivity to the mantle flow pattern and the dynamic topography.

2. Methods -data processing
2.1 Data sets & Trajectories computation

We use one of the latest version of the global Earth topography at 30s resolution, SRTM30 Plus V6.0 (Becker et al., 2009), based on the compilation of land topography and ocean bathymetry inferred from a new satellite-gravity model, available at UCSD website[1]. Topography is corrected from sediment loading by considering the most recent sediment thickness grid[2] (Divins, 2012). Any reference to bathymetry or topography in the following refers to the corrected bathymetry.

For the age of the ocean floor we use the 2' age grid from Müller et al. (2008), version 3.2[3]. In the following, all grids will be considered at 2' resolution, which is the best available resolution common to all datasets. Plate boundaries, and in particular ridges location, are taken from the compilation and electronic files of Bird (2003). The maps

[1] http://topex.ucsd.edu/WWW_html/mar_topo.html
[2] http://www.ngdc.noaa.gov/mgg/sedthick/sedthick.html
[3] http://www.ngdc.noaa.gov/mgg/ocean_age/data/2008/grids/age/

displayed in this article are plotted with the Generic Mapping Tools (GMT) software (Wessel and Smith, 1991).

Age trajectories are computed from recently published rotation poles (Müller et al., 2008). They are computed from each main mid-ocean ridge, on each neighboring plate. For this purpose, the ridges coordinates (Bird, 2003) have been resampled every 10km for each main ocean. We considered 1370 trajectories over the Pacific plate, 555 over the Nazca plate, 600 for the South America plate, 700 over the North America plate, 780 over the Eurasia plate, 760 over the Nubia plate and 768 over the India plate. Along these trajectories, we investigate the relationship between the seafloor depth and its age. The age trajectories along which we derive the bathymetry trend are displayed in Figure 1. In order to illustrate this study and provide an even coverage and outlook on all the plates, we have displayed only one profile out of 100.

2.2 Fit of the bathymetry trend

There are several studies that statistically assess the variation of the subsidence parameters (Kane and Hayes, 1994a,b; Perrot et al., 1998; Hillier and Watts, 2005). Perrot et al. (1998) perform a linear regression between the bathymetry and the square root of the seafloor age. The problem with this approach is that several geological features such as volcanoes and swells are superimposed of the subsidence trend. Therefore the derived subsidence trend tends to be shallower than the actual one. Other approaches filter out the geological features before deriving the bathymetry versus square root of the seafloor age fit (Hillier and Watts, 2005). However in their method the parameters have to be locally adjusted and have a non-negligible influence on the retrieved trend. In the following we propose two independent methods for deriving the subsidence parameters.

The outliers method

Our purpose is to extract the linear trend between the bathymetry and the square-root of age along the age trajectories. As stated earlier, bathymetry profiles contain many geologic features such as seamounts, hotspot swells, fracture zones, etc., which should not be taken into account in this linear regression. Rather than manually removing the corresponding zones, as was done previously in the literature, we chose to develop a method that makes it possible to capture the general bathymetric trend with a simple linear regression, without the bias introduced by the presence of outliers. The principle of the outliers method is to provide a linear fit (between the bathymetry and the square-root of age for example) assuming that there are positive outliers (Rousseeuw and Leroy, 1987). This method is a method classically used in data processing, but has rarely been applied for the treatment of geophysical data. We adapt it to the present problem. A full description of this method is provided in the SOM (Supplementary Online Material). The only parameter is the outlier range, M_0, which we fix at 1000 m, the range of the

geological features representing the outliers. There are no noticeable alterations of the final fit if this parameter varies in the range of 500 to 5000 m for example.

Along each profile there is a linear relation between the bathymetry and the square root of the seafloor age, up to a point, hereafter named "inflexion point", where the bathymetry departs from the linear trend and never recovers it. The outliers fit of the linear trend provides the fitted ridge's depth, Z_R, and the subsidence rate, τ. The subsidence rate is the deepening of the seafloor, w, from the ridge, where the depth of the seafloor is Z_R (the fitted depth), until the inflexion point, where the seafloor depth is Z_i, divided by the square root of seafloor's age at this same point.

$$\tau = \frac{z_R - z_i}{\sqrt{age}} = \frac{w}{\sqrt{age}} \quad (1)$$

The fits obtained with the outliers method are displayed in Fig. 2. The arrow at the end of the profiles represent the inflexion point. We also report the seafloor age at this location. We have displayed only one profile for each lithospheric plate, but in the SOM, the fit of the subsidence trend is provided for one profile out of 100 for each ocean (fig. S1).

MiFil

In order to ensure that the variation of the obtained subsidence parameters is not an artifact of the outliers method, we choose to derive these parameters using another method, completely independent of the previous one. Within this method, geological features such as volcanoes and swells superimposed on the subsidence trend are removed through the MiFil method. The MiFil method (for Minimization and Filtering) is a filtering method especially designed for the characterization of depth anomalies (Adam et al., 2005). It requires two stages: the first is to approximately remove the island/volcanic component of topography by minimizing the depth anomaly. During the second stage, the minimized grid is filtered through a median filter in order to smooth the shape and totally remove the remaining small spatial length scale topography. The strength of this method is that it does not require any assumption on the location, amplitude, or width of the large-scale feature to characterize. The filtering parameters, i.e. the radii of the minimizing and median filters (hereafter r and R respectively), are computed by considering the spatial length scale of the features to remove. Previous studies pointed out that the volcanoes and swells associated with hotspot chains are completely removed for the radii r=50 km and R=700 km (Adam and Bonneville, 2005). More details on the MiFil method, and the study of the sensitivity to the parameters are provided in the SOM. In the following we will only consider the subsidence parameters obtained with these parameters. Once the geological features are removed, we perform a linear regression between the filtered bathymetry and the square root of the seafloor age. We then derive the subsidence rate, τ, and the seafloor's depth at the ridge, Z_R, fitted from our regression.

3. Results of the bathymetry fits
3.1 Subsidence parameters

The subsidence parameters (ridge height and subsidence rate) are displayed in Fig. 3 for each major oceanic plate. The parameters obtained with the outliers method are reported in blue, the parameters obtained with MiFil in red. The subsidence rate is plotted in the left side panels. Both the methods lead to similar results, with a subsidence rate varying between 100 and 500 m $Myr^{-1/2}$. The spatial evolution found through the two independent methods is nearly identical. It seems actually that the parameters found through the MiFil method are a low pass filter of the ones found with the outliers method. This is expected because with MiFil we filter out the small wavelength features on a 2D grid. The fact that similar values of the subsidence rate are found through two independent methods indicates that the variation of these parameters are not artifacts of the employed methods. These parameters are robust.

The variation of ridge depth, Z_R, is displayed in the right side panels. We reported in black the bathymetry interpolated along the mid-oceanic ridge. Here again, the values of Z_R found with the outliers method are similar to the ones found with the MiFil method. The values found with the outliers method are generally larger. This is intrinsic to the methods and has been illustrated in the SOM. The values of the bathymetry (black dots) generally lie between the two estimates, except for some local departures which may be explained by the presence of known geological features. For example, around latitude 0º in the west Pacific, the bathymetry values are larger than the ones determined by the fitting. This may be due to what is occurring on the eastern side of the EPR. The Cocos ridge may indeed contribute to the elevation of the ridge but may not significantly affect the seafloor west of the EPR, where the fits have been performed.

3.2. Importance of the direction along which the subsidence is studied

Previous studies have pointed out the importance of considering the seafloor subsidence not along age trajectories, but rather along flow lines, i.e. trajectories along the present-day plate motion direction (Adam and Vidal, 2010). In this article, we focus on the scaling of the seafloor depth as a function of the square root of age, for young ages, in the range of 0-50 Ma. This section demonstrates that in this range, the direction along which the subsidence is studied does not play a major role for the determination of the subsidence parameters.

The flow lines are computed using the global set of relative plate angular velocities estimated by Gripp & Gordon (2002), in the reference frame HS3-NUVEL1a. Several kinematic velocities from different models have been tested. On the Pacific plate, the flow lines remain almost unchanged. However, the kinematics – and thus, the associated flow lines – of slower plates can be strongly affected by the choice of the kinematic model. The choice of HS3-NUVEL1a was mainly motivated by the fact that it is a standard to compute plate velocities. With the available rotation poles, we cannot

compute realistic flow lines for very slow plates such as Antarctica, Eurasia or Nubia. The flow lines are represented in Fig. 4 a) (in red), at the same time as the age trajectories previously discussed (in black). Along the flow lines, we interpolate the age of the seafloor and perform, as earlier, a linear regression between the bathymetry and the square root of the seafloor age through the outliers method. As previously, the linear fit is not recovered along the whole trajectories. The parameters displayed here have been obtained in the 0-50 Ma age range. They remain roughly the same if we slightly modify this age range, if one considers for example the 0-40 or 0-60 Ma age range.

The parameters we obtain are displayed in Fig. 4, in panels b) to i), in red. We also report in black the parameters derived along the age trajectories with the outliers method. The variation of these parameters from both the sets of trajectories is quite similar. Yet, the angle between these trajectories is as high as 40° in the Pacific and West Atlantic oceans. We conclude that the direction along which the subsidence is studied does not have a major importance as long as the angle between the considered trajectories is 40-50° or less, and the study concerns mainly young seafloor (ages < 50 Ma).

3.3. Effective thermal conductivity

One physical interpretation of the variation of the subsidence rate is variations in the lithospheric properties expressed by variations in the effective thermal conductivity. These quantities are related by the following equation (Turcotte and Schubert, 2002) :

$$w = \frac{2 \rho_m \alpha_v z_R (T_m - T_0)}{\rho_m - \rho_w} \sqrt{\frac{K\,age}{\pi}} \quad (2)$$

where w is the deepening of the seafloor, ρ_m and ρ_w the mantle and sea water densities ($\rho_m = 3350$ kg m^{-3} and $\rho_w = 1050$ kg m^{-3}), T_m and T_0 the mantle and sea water temperatures ($T_m - T_0 = 1300$ K), α_v the coefficient of thermal expansion ($\alpha_v = 3.10^{-5}$ K^{-1}), age the seafloor age, and K the thermal diffusivity which can be expressed as $K = \frac{k_{eff}}{\rho_m c}$ where c is the specific heat ($c = 1$ kJ kg^{-1} K^{-1}) and k_{eff} the effective thermal conductivity we are computing here. Because our fits provide the subsidence rate (see eq. 1), the determination of the effective thermal conductivity is straightforward. The variation of the effective thermal conductivity, k_{eff}, computed from the bathymetry fits along age trajectories with the outliers method is represented in black in the uppermost panels of fig. 5 b), c), d).

The classical value of the thermal conductivity of the oceanic lithosphere, in agreement with its structure is $k_{eff} \approx 3$ Wm^{-2}. Departures from this value have been interpreted in terms of mantle temperature (Kane and Hayes, 1994a;b), or as the variation of the temperature-pressure-dependent thermal properties (such as basal temperature,

asymptotical plate's thickness, thermal expansivity), axial hydrothermal circulation, and oceanic crust (Grose and Afonso, 2013; Hillier and Watts, 2005). Although some of these variations indirectly take into account the variation of the mantle properties, none of the previous studies has directly taken into account the mantle dynamics, as we are doing in the present study.

4. Mantle dynamics
4. 1 Instantaneous mantle flow model

To account for the dynamic flow of the mantle, we compute the instantaneous flow based on the S40RTS tomography model (Ritsema et al., 2010). We convert the seismic velocities anomalies into density anomalies and model the instantaneous flow they induce by solving the conservation equations of mass and momentum in a global 3D spherical shell geometry. A complete description of the numerical model, as well as a discussion on the parameters influence is provided in the SOM. In the following we present the results obtained with a depth and temperature dependent viscosity, where the temperature dependency is introduced through an Arrhenius-type law, and the depth dependency imposes a lower mantle 100 times more viscous than the upper mantle. In order to recover the lithospheric plate's motion, we also impose weak plate boundaries at the surface and introduce the regionalized upper mantle (RUM) slab model of Gudmundsson and Sambridge (1998) with a density of 50 kg m^{-3}. For the continents we impose a null density between depths 0 and 300 km. Depth-cross sections and maps of the modeled convection pattern are provided in fig. 5 and 6.

4.2 Mantle dynamics and effective thermal conductivity

As stated earlier, a physical interpretation of the variations of the subsidence rate is the effective thermal conductivity (see section 3.3). In fig. 5 we compare the convection pattern computed from the tomography model and the effective thermal conductivity, k_{eff}, computed from the bathymetry fits. In panel a) we display the profiles along which we investigate the convection pattern. In panels b), c), d), the uppermost panels report the variation of k_{eff} along the main mid-oceanic ridges, and the lowermost panels the convection pattern beneath them. The rest of the panels show the convection pattern across the main oceanic plates.

In fig. 6, we report the convection pattern at 200 km depth. In the Pacific ocean it reflects at a large scale the upwelling of the South Pacific Superswell (fig. 6 a) and b)), which creates a radial upwelling centered at longitude 210°E and latitude 15°S, with a smaller upwelling centered near Hawaii (longitude 207°E and latitude 20°N). The pattern associated with the upwelling of the South Pacific superplume extends along almost half of the Pacific plate. In the Eastern Pacific, this flow extends to the EPR and opposes the lithospheric plate motion, a phenomenon previously pointed out by Gaboret et al. (2003). This flow impacts the mid-oceanic ridge between latitudes 35°S and 20°N, and is clearly observed in profile P3 (Fig. 5 g)). This generates dynamic topography

with a maximum amplitude in the South Central Pacific, which continuously decreases away from it. In the vicinity of the EPR, the slope of the dynamic topography has a sign opposite to the one created by the subsidence of the oceanic seafloor. It is then not surprising that the region encompassed between latitudes 35°S and 20°N along the Pacific ridge is characterized by low k_{eff}.

South of latitude 35°S, the effective thermal conductivities are slightly larger than 3 Wm^{-1}K^{-1}. This may be due to the presence of the Foundation, Louisville and Balleny hotspots. We see indeed a local upwelling along the P4 profile (fig.5 h). In the same way, there seems to be a local upwelling north of the Pacific plate, along the P1 profile (fig. 5 e) which may be related to the Soccorro or Baja hotspots or to local mantle anomalies. In this region the effective thermal conductivities are also slightly larger than 3 Wm^{-1}K^{-1}.

In the Indian and Atlantic oceans, the variations of effective thermal conductivity are mainly associated with hotspots. For example, high k_{eff} are found for Iceland and the Azores where we model upwelling flows created by hot mantle anomalies, displayed respectively on the profiles A1 and A3 in fig. 5 i) and k). In between these hotspots, our model recovers downwellings created by a relatively cooler mantle (profile A2 in fig. 5 j)). These downwelling flows are associated with low k_{eff}. Near the South African superswell, we seem to recover a pattern similar to the one observed in the Pacific (profile A4 fig. 5 l)). The upwelling of the South Africa Superplume occurs at longitude 20°E. The convection cell it creates dives back into the mantle near the MAR, around longitude 12°W. Low k_{eff} are recovered over this region. Further south, near the Walvis chain, the model recovers a local shallow upwelling associated with a locally hotter mantle, superimposed on the South Africa Superplume return flow (profile A5 fig. 5 m)).

In the South-East Indian ocean two major mantle upwellings occur near the locations of St. Paul Amsterdam, north-west and Balleny, south-east (fig. 6 d), fig. 5 d)) and profiles I1 and I3 of fig. 5 n) and p)). In between these upwellings, a large scale dowelling is found in the whole mantle at the Antartic-Autralia Discordance (AAD) (fig. 5 d) and 6d)). This section of the South-East Indian mid-oceanic ridge (SEIR) is very peculiar. From geophysical observations, it appears to be a very cold ridge and has the characteristics of a slow spreading ridge (e.g. great thrust faults), although the spreading rates are high to moderate. Here again, the modeled mantle upwellings are associated with high k_{eff}, and low k_{eff} are found along the AAD.

5. Dynamic topography

A more quantitative way to consider the mantle dynamics is through the computation of the dynamic topography, i.e. the stress field generated at the surface by the instantaneous mantle flow. The derivation of the dynamic topography and a discussion of the influence of the model's parameters are provided in the SOM. Here we only present the results obtained through the best fitting model, previously described. The

dynamic topography is displayed in Fig. 7 a). The amplitude of the dynamic topography presents a maximum along mid-oceanic ridges. The amplitude decreases while increasing the distance from the ridge. To allow a visual comparison between the bathymetry and the dynamic topography, we display these models along trajectories crossing the major oceans (Fig. 7 b) to g); more profiles are available in the SOM). The long wavelength subsidence trend observed in the bathymetry is well retrieved by the dynamic topography. In order to investigate more quantitatively the correlation between the subsidence trend observed in the bathymetry and the dynamic topography, we compute the subsidence parameters from the dynamic topography and compare them to the ones derived from the bathymetry.

6 Subsidence parameters deduced from the dynamic topography

The subsidence parameters from the dynamic topography are computed in a process similar to that used for the bathymetry, i.e. we perform a linear regression between the dynamic topography and the square root of the seafloor age along the age trajectories. However, recovering the subsidence parameters, and especially the subsidence rate from the dynamic topography is quite challenging. The main reason is the low resolution of the tomography model. The S40RTS tomography model includes spherical harmonics up to degree and order 40, which implies a resolution of roughly 1000 km. On fig 7 c), one can see for example that the Hawaiian swell is well recovered. But the Hawaiian swell is one of the biggest hotspot swells on Earth (King and Adam, 2014). Generally the wavelength of the other intraplate features observed in the bathymetry is much shorter. The dynamic topography recovered along these smaller features has a wavelength that is greater than the one observed in the bathymetry. Therefore, the filtering methods developed for the bathymetry are less efficient to derive the subsidence pattern from the dynamic topography. Indeed, along most of the profiles, the wavelength of the dynamic topography associated with mantle upwelling (or downwellings) is roughly one third of the subsidence trend (see SOM). In such cases, it proves fundamentally difficult to isolate the subsidence trend. This shortcoming can be resolved by improving the resolution of the tomography models.

In fig. 8, we compare the subsidence rate deduced from the bathymetry (in black and blue) to the subsidence rate deduced from the dynamic topography (in red). We highlighted in gray the areas where the profiles are shorter than 3000 km, and therefore do not allow a correct fit of the dynamic topography. We can see that for regions for which the age trajectories are long enough, the major tendencies isolated from the bathymetry are recovered from the dynamic topography.

Ideally the subsidence parameters should be recovered with the same dynamic model in all the oceans. This is not the case. Indeed, for the Atlantic and Indian oceans, the subsidence rate derived from dynamic topography has to be multiplied by a factor two in order to match the subsidence rate derived from bathymetry. We investigated several viscosity laws and several laws to convert velocities anomalies into density anomalies.

None of the considered models allowed us to reproduce the subsidence rate for all the oceans simultaneously. Maybe more complex rheologies, considering the composite viscosities laws based on diffusion creep and dislocation creep viscosities (Lee and King, 2011) should be introduced in further studies. However, rheology may not the major factor here. Indeed, the pattern and amplitude of the available tomography models still show noticeable differences (Schaeffer and Lebedev, 2013). These differences are even more significant when anisotropy is considered (Zhou et al., 2006; Montagner, 2002). Furthermore, other studies show that ignoring the anelastic dispersion in surface waves inversions can lead to biased tomography models (Dalton et al., 2008; Ruan and Zhou, 2012) are considered. The difference of the considered tomography models has a non-negligible influence on the inferred dynamic model (Becker and Boschi, 2002). More tomographic models have to be investigated in order to see if the fact that we cannot reproduce the subsidence parameters simultaneously for all the oceans comes from our design of the dynamic model or from the input tomography model.

The resolution of the tomography models may also be an important factor. An intriguing fact is that the vertical resolution at 150 km depth of the S20RTS model, the previous version of the S40RTS model is 120 km in the south Atlantic and Indian oceans, whereas it is roughly the half in the Pacific ocean (see fig. 1 in Ritsema et al. (2007)), where we do not need a multiplicative factor to reproduce the subsidence rates. The improvement of the lateral resolution may also facilitate to study of the subsidence pattern from dynamic topography. At this point there are few trajectories in the Atlantic ocean and none in the Indian ocean that are long enough to allow a reliable fit of the subsidence pattern from the dynamic topography. So far, the best place to study the subsidence pattern from tomography models is the Pacific ocean. The dynamic model we designed provides a good quantitative explanation for the variation of the subsidence parameters. Indeed, as we show in fig. 8, the subsidence rate derived from the dynamic topography reproduces well the subsidence rate derived from the bathymetry. In fig. 9 we also investigate the correlation between the ridge depth (in black and blue) with the dynamic topography along mid-oceanic ridges (in red). Except some local departures the ridge depth variations are well reproduced by the dynamic model. In conclusion, our dynamic model provides a satisfactory quantitative explanation of the subsidence parameters derived from bathymetry.

These results do not prove that the deepening of the seafloor is a dynamic phenomenon, as opposed to a passive phenomenon due to the conductive cooling of the lithosphere after its creation at mid-oceanic ridges. Indeed the seismic waves reproduce the thickening of the lithosphere, and our dynamic model is based on the density anomalies derived from this configuration. Therefore the isostatic component (Turcotte and Schubert, 2002) is indirectly introduced in our model. However, based on the density anomalies derived from tomography models, it is impossible to recover the subsidence pattern according to the isostatic hypothesis. This could indicate that subsidence of the seafloor is induced by the combination of static and dynamic phenomena. This consideration is beyond the scope of this paper, although it deserves further

investigations. The main point of this study is that departures of the 'normal' subsidence, characterized by k_{eff}=3 Wm^{-1}K^{-1} (which corresponds to a subsidence rate of 300 m/Myr^{-1}) are induced by the mantle dynamics. The dynamic model we designed provides a satisfactory explanation of the variation of the subsidence parameters deduced from bathymetry.

7. Discussion and conclusion

We conducted a statistical study of the seafloor subsidence parameters, using the latest and more accurate data sets. From recently published rotation poles we computed age trajectories for all the major oceanic plates. More than 5.000 trajectories have been computed, providing complete global coverage. Along these trajectories we determine the subsidence parameters (ridge depth and subsidence rate) through two independent methods. The variations of the obtained parameters are insensitive to the fitting method, thus demonstrating the robustness of our results. Moreover, the direction along which the subsidence is studied does not seem to be important. The subsidence parameters display great variation, with the subsidence rate varying between 50 and 800 m Ma$^{-1/2}$ and, and the ridge depth between a few hundred meters and 5000 m. To account for these variations we model a instantaneous flow model, in a global 3D spherical shell geometry, based on the S40RTS tomography model.

We show that departures from the effective thermal conductivity value, k_{eff}=3 Wm^{-1}K^{-1} are systematically related to the mantle convection pattern. Regions associated with low values of k_{eff} are associated with mantle downwellings, whereas high values of k_{eff} are found in regions associated with mantle upwelling. The most striking result is that these flows are not local phenomena, but generally involve regions larger than 10.000 km. The return flows of the South Pacific and African superswells seem to descend back in the mantle in the vicinity of the EPR and the MAR, thus regionally deflecting downward these mid-oceanic ridges, between latitudes 35ºS and 10ºN, and 55ºS and 30ºS respectively. The characteristics of the Antartic-Autralia Discordance, which appears to be a very cold ridge and has the characteristics of a slow spreading ridge (e.g. great thrust faults), although the spreading rates are high to moderate, can also be explained by a large scale downwelling flow, which seems to be the return flow created by the upwelllings occurring east and west of this region, in the vicinity of the Balleny and St. Paul Amsterdam hotpots. This demonstrates that the mantle dynamics plays a major role in the shaping of the oceanic seafloor. In particular, the parameters generally considered to quantify the lithosphere structure, such as the thermal conductivity, are not only representative of this structure but mainly incorporate signals from the mantle convection occurring beneath the lithosphere.

Small variations of k_{eff} can be accounted for by the variation of the temperature-pressure-dependent thermal properties (such as basal temperature, asymptotical plate's thickness, thermal expansivity), or the structure of the oceanic crust, as pointed out by previous authors (Hillier and Watts, 2005; Grose and Afonso, 2013). But values as low

as k_{eff}=1 Wm^{-1}K^{-1} are unlikely to be accounted for by such variations. The plausible explanations include deeper phenomena or hydrothermal circulation. It is unclear why this latter would occur preferentially in some locations rather than in others, or deeper phenomena. We show here that these variations are related to the mantle structure and dynamics.

For the subsidence rate, the major tendencies isolated from the bathymetry are well recovered from the dynamic topography. The determination of the subsidence trend from the dynamic topography is not accurate along short profiles (shorter than 3000 km, areas highlighted in gray). Considering the simplistic way the lithosphere is described in our model, the correlation between these subsidence rates derived from the bathymetry and the dynamic topography is actually surprisingly good. Overall we find a good correlation between the subsidence parameters derived from the bathymetry and the dynamic topography. This points out to the fact that these parameters are strongly dependent on mantle dynamics.

Figures' caption

Figure 1: Emplacement of the age trajectories on the bathymetry (a) and seafloor age map (b). Along the profiles represented in white we are displaying the subsidence pattern (Fig. 2).

Figure 2: Fit of the bathymetry versus the square root of the seafloor age for the major oceanic plates. a) the Pacific plate, b) Nazca plate, c) south America, d) Nubia, e) Indian plate, computed with the outliers method (see text). The emplacement of the trajectories is represented in Figure 1. The arrow at the end of the profiles is the departure point defined as the location from where the bathymetry departs from the linear trend versus the square root of the seafloor age and never recovers it. We report the age of the departure from the linear trend in Ma above the arrow.

Figure 3: Subsidence parameters (subsidence rate and ridge height) determined with the outliers method (in blue) and with the MiFil method (in red) for the major oceanic plates as a function of the mid-oceanic ridges' latitude or longitude. In the ridge depth panels (Z_R), we also report in black the bathymetry interpolated along the mid-oceanic ridges.

Figure 4: Study of the importance of the directivity along which the subsidence parameters are studied. We compare the subsidence parameters determined along the age trajectories (in black) and flow lines (in red). These two sets of trajectories are represented in panel a). Panels b) to i) show the subsidence parameters determined with the outliers method along the age trajectories (black dots) and along the flow lines (red dots).

Figure 5: Effective thermal conductivity and flow pattern. a) bathymetry map where we display the profiles along which we investigate the convection pattern. The profiles in black cross the oceanic plates and the red lines are the mid-oceanic ridges. The emplacement of hotspots are reported by the red stars (from King and Adam (2014)). In the other panels, the color-map represents the density anomalies deduced from tomography models and the arrows the convection driven by these anomalies. In panels b, c, d, the uppermost panels report the variation of k_{eff} along the main mid-oceanic ridges.

Figure 6: Flow pattern computed from the S40RTS tomography model at 200 km depth. The emplacement of hotspots are reported by the red stars (from King and Adam (2014)).

Figure 7: Subsidence trend and dynamic topography. In the uppermost panel, we display the derived dynamic topography and the emplacement of the profiles along which we investigate the correlation between the bathymetry and the dynamic topography. The mid-oceanic ridges are reported in blue. In panels a) to g), the black lines represent the bathymetry, and the red lines the dynamic topography.

Figure 8: Subsidence rates derived from the dynamic topography, in red, compared to the subsidence rates deduced from the bathymetry (in blue with MiFil, in black with the outliers method). The subsidence rates deduced from the dynamic topography for the Atlantic and Indian oceans have been multiplied by a factor two in order to match the subsidence rates deduced from bathymetry (see discussion in the text).

Figure 9: Ridge depth variation derived from the dynamic topography, in red, compared to the ridge bathymetry: in black observed bathymetry, in blue, ridge depth obtained by fitting through MiFil.

References

Adam C., V. Vidal and A. Bonneville (2005), MiFil: a method to characterize hotspot swells with application to the South Central Pacific, Geochem. Geophys. Geosyst., 6, Q01003, doi:10.1029/2004GC000814

Adam C. and A. Bonneville (2005) , Extent of the South Pacific Superswell, J. Geophys. Res., 110, B09408, doi:10.1029/2004JB00346

Adam, C., and V. Vidal (2010), Mantle Flow Drives the Subsidence of Oceanic Plates Science **328**, 83-85.

Becker, T. W. and Boschi, L. (2002), A comparison of tomographic and geodynamic mantle models, Geochem., Geophys., Geosys., 3(1), 1003, doi:10.1029/2001GC000168.

Becker, J. J., D. T. Sandwell, W. H. F. Smith, J. Braud, B. Binder, J. Depner, D. Fabre, J. Factor, S. Ingalls, S-H. Kim, R. Ladner, K. Marks, S. Nelson, A. Pharaoh, G. Sharman, R. Trimmer, J. VonRosenburg, G. Wallace, and P. Weatherall (2009), Global Bathymetry and Elevation Data at 30 Arc Seconds Resolution: SRTM30_PLUS, Marine Geodesy, **32**:4, 355-371.

Bird, P. (2003), An updated digital model of plate boundaries, Geochem. Geophys. Geosyst., **4**(3), 1027.

Calcagno, P., and A. Cazenave (1994), Subsidence of the seafloor in the Atlantic and Pacific Oceans: Regional and large-scale variations, Earth Planet. Sci. Lett., **126**, 473-492.

Dalton, C. A., G. Ekström, and A. M. Dziewoóski (2008), The global attenuation structure of the upper mantle, J. Geophys. Res., 113, B09303, doi:10.1029/2007JB005429.

Divins, D.L. (2012), NGDC Total Sediment Thickness of the World's Oceans & Marginal Seas, http://www.ngdc.noaa.gov/mgg/sedthick/sedthick.html

Gaboret, C., A. Forte, and J.-P. Montagner (2003), The unique dynamics of the Pacific hemisphere mantle and its signature on seismic anisotropy, *Earth Planet. Sci. Lett.*, *208*(3), 219–233.

Gripp, A. E., and R. G. Gordon (2002), Young tracks of hotspots and current plate velocities, Geophys. J. Int. **150**, 321-361.

Grose, C. J., and J. C. Afonso (2013), Comprehensive plate models for the thermal evolution of oceanic lithosphere, Geochem. Geophys. Geosyst., 14, 3751–3778, doi:10.1002/ggge.20232.

Gudmundsson, O., and M. Sambridge (1998), A regionalized upper mantle (RUM) seismic model, J. Geophys. Res., **103**, 7121-7136.

Hillier, J.K., Watts, A.B. (2005), Relationship between depth and age in the North Pacific Ocean. J. Geophys. Res. 110, B02405.

Kane, K., and D. Hayes (1994a), Long-lived mid-ocean ridge segmentation: Constraints on models, J. Geophys. Res., **99**, 19,693-19,706.

Kane, K., and D. Hayes (1994b), A new relationship between subsidence rate and zero-age depth, J. Geophys. Res., **99**, 21,759-21,777.

King S. D. and C. Adam (2014), Hotspot swells revisited, Physics of the Earth and Planet. Int., 235, 66–83

Klein, E. M., and C. H. Langmuir (1987), Global correlations of ocean ridge basalt chemistry with axial depth and crustal thickness, J. Geophys. Res., **92**, 8089-8115.

Lee, C., and S.D. King (2011), Dynamic buckling of subducting slabs reconciles geological and geophysical observations, Earth Planet. Sci. Lett., 312, 360–370

Marty, J. C., and A. Cazenave, (1989), Regional variations in subsidence rate of oceanic plates: a global analysis, Earth Planet. Sci. Lett. **94**, 301-315.

Montagner, J-P (2002), Upper mantle low anisotropy channels below the Pacific plate, Earth Planet. Sci. Lett., 202, 263–274.

Müller, R. D., M. Sdrolias, C. Gaina, and W. R. Roest (2008), Age, spreading rates, and spreading asymmetry of the world's ocean crust, Geochem. Geophys. Geosyst., **9**, Q04006.

Niu, Y., and M. J. O'Hara (2008), Global correlations of ocean ridge basalts chemistry with axial depth: a new perspective, J. Petrol. **49**, 633-664.

Perrot, K., J. Francheteau, M. Maia, and C. Tisseau (1998), Spatial and temporal variations of subsidence of the East Pacific Rise (0-23ºS), Earth Planet. Sci. Lett., **160**, 593-607.

Ritsema, J., McNamara, A.K., Allen, K., Bull, A.L. (2007), Tomographic filtering of geodynamic models: implications for model interpretation and large-scale mantle structure. J. Geophys. Res. 89 (112), B1.

Ritsema, J., Deuss, A., van Heijst, H.J., Woodhouse, J.H. (2010), S40RTS: a degree-40 shear-velocity model for the mantle from new Rayleigh wave dispersion, teleseismic traveltime and normal-mode splitting function measurements. J. Int. Geophys., 10.1111/j.1365-246X.2010.04884.x.

Rousseeuw R.J., and A.M. Leroy (1987), Robust Regression and Outlier Detection, Wiley

Ruan Y. and Y. Zhou (2012), The effects of 3-D anelasticity (Q) structure on surface wave amplitudes, Geophys. J. Int. 189, 967–983

Schaeffer A. J. and S. Lebedev (2013), Global shear speed structure of the upper mantle and transition zone, Geophys. J. Int., doi: 10.1093/gji/ggt095

Turcotte, D.L., Schubert G., 2002. Geodynamics, 2nd edition, Cambridge Univ. Press, pp. 456.

Wessel, P., Smith, W.H.F. (1991), Free software helps map and display data. EOS Trans. AGU 72, 441–446.

Zhou, Y., G. Nolet, F. A. Dahlen, and G. Laske (2006), Global upper-mantle structure from finite-frequency surface-wave tomography, J. Geophys. Res., 111, B04304, doi:10.1029/2005JB003677.

Figure's captions

Figure 1: Emplacement of the age trajectories on the bathymetry (a) and seafloor age map (b). Along the profiles represented in white we are displaying the subsidence pattern (Fig. 2).

Figure 2: Fit of the bathymetry versus the square root of the seafloor age for the major oceanic plates. a) the Pacific plate, b) Nazca plate, c) south America, d) Nubia, e) Indian plate, computed with the outliers method (see text). The emplacement of the trajectories is represented in Figure 1. The arrow at the end of the profiles is the departure point defined as the location from where the bathymetry departs from the linear trend versus the square root of the seafloor age and never recovers it. We report the age of the departure from the linear trend in Ma above the arrow.

Figure 3: Subsidence parameters (subsidence rate and ridge height) determined with the outliers method (in blue) and with the MiFil method (in red) for the major oceanic plates as a function of the mid-oceanic ridges' latitude or longitude. In the ridge depth panels (Z_R), we also report in black the bathymetry interpolated along the mid-oceanic ridges.

Figure 4: Study of the importance of the directivity along which the subsidence parameters are studied. We compare the subsidence parameters determined along the age trajectories (in black) and flow lines (in red). These two sets of trajectories are represented in panel a). Panels b) to i) show the subsidence parameters determined with the outliers method along the age trajectories (black dots) and along the flow lines (red dots).

Figure 5: Effective thermal conductivity and flow pattern. a) bathymetry map where we display the profiles along which we investigate the convection pattern. The profiles in black cross the oceanic plates and the red lines are the mid-oceanic ridges. The emplacement of hotspots are reported by the red stars (from King and Adam (2014)). In the other panels, the color-map represents the density anomalies deduced from tomography models and the arrows the convection driven by these anomalies. In panels b, c, d, the uppermost panels report the variation of k_{eff} along the main mid-oceanic ridges.

Figure 6: Flow pattern computed from the S40RTS tomography model at 200 km depth. The emplacement of hotspots are reported by the red stars (from King and Adam (2014)).

Figure 7: Subsidence trend and dynamic topography. In the uppermost panel, we display the derived dynamic topography and the emplacement of the profiles along which we investigate the correlation between the bathymetry and the dynamic topography. The mid-oceanic ridges are reported in blue. In panels a) to g), the black lines represent the bathymetry, and the red lines the dynamic topography.

Figure 8: Subsidence rates derived from the dynamic topography, in red, compared to the subsidence rates deduced from the bathymetry (in blue with MiFil, in black with the outliers method). The subsidence rates deduced from the dynamic topography for the Atlantic and Indian oceans have been multiplied by a factor two in order to match the subsidence rates deduced from bathymetry (see discussion in the text).

Figure 9: Ridge depth variation derived from the dynamic topography, in red, compared to the ridge bathymetry: in black observed bathymetry, in blue, ridge depth obtained by fitting through MiFil.

Figure 1
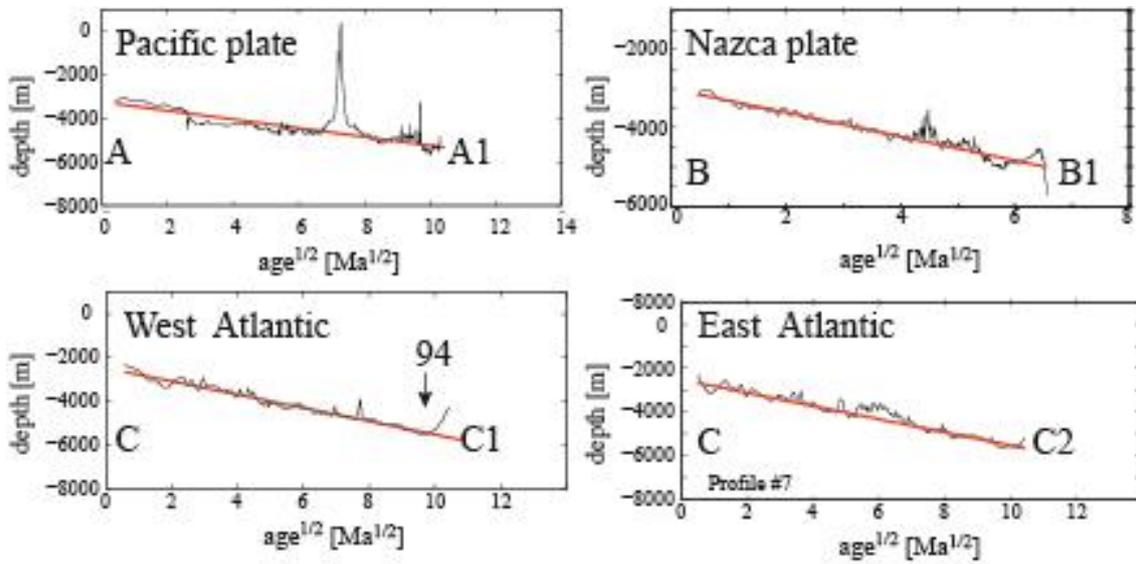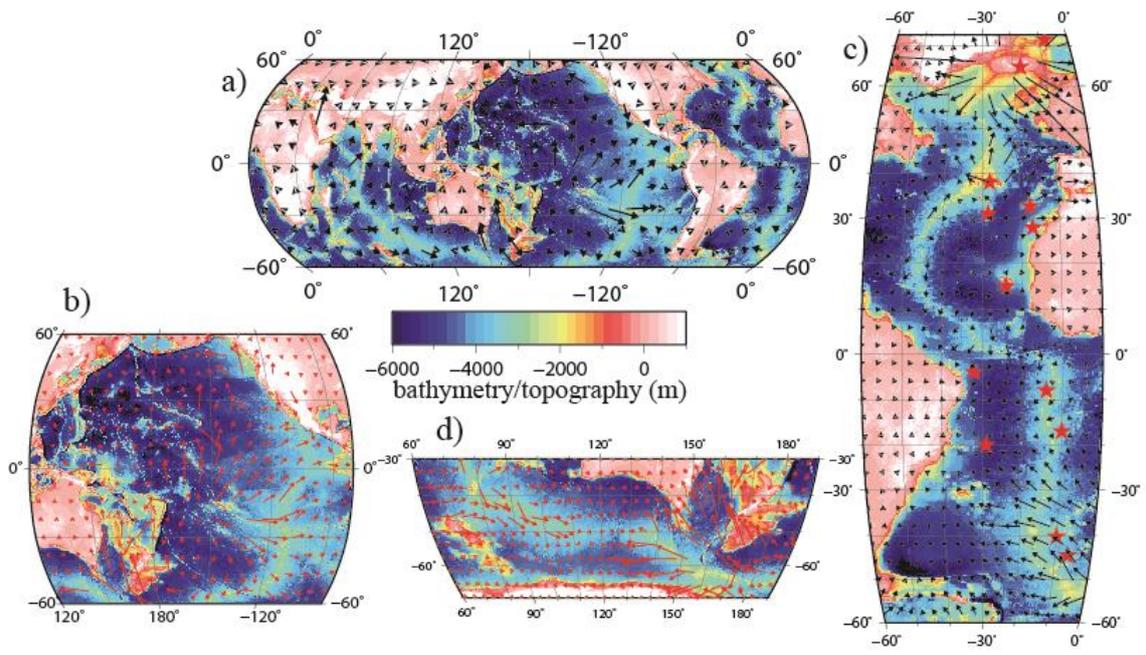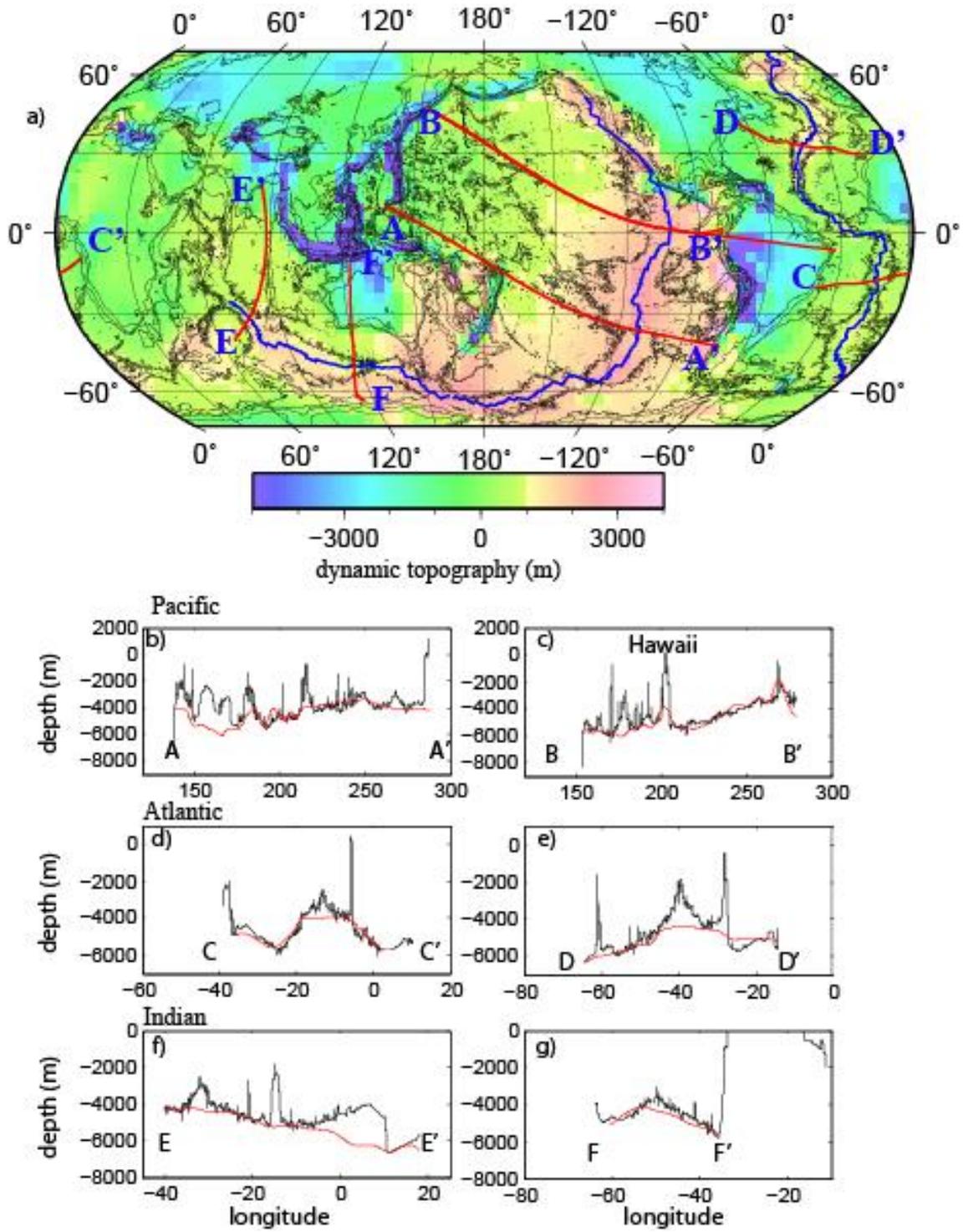
Indian!

Figure 2
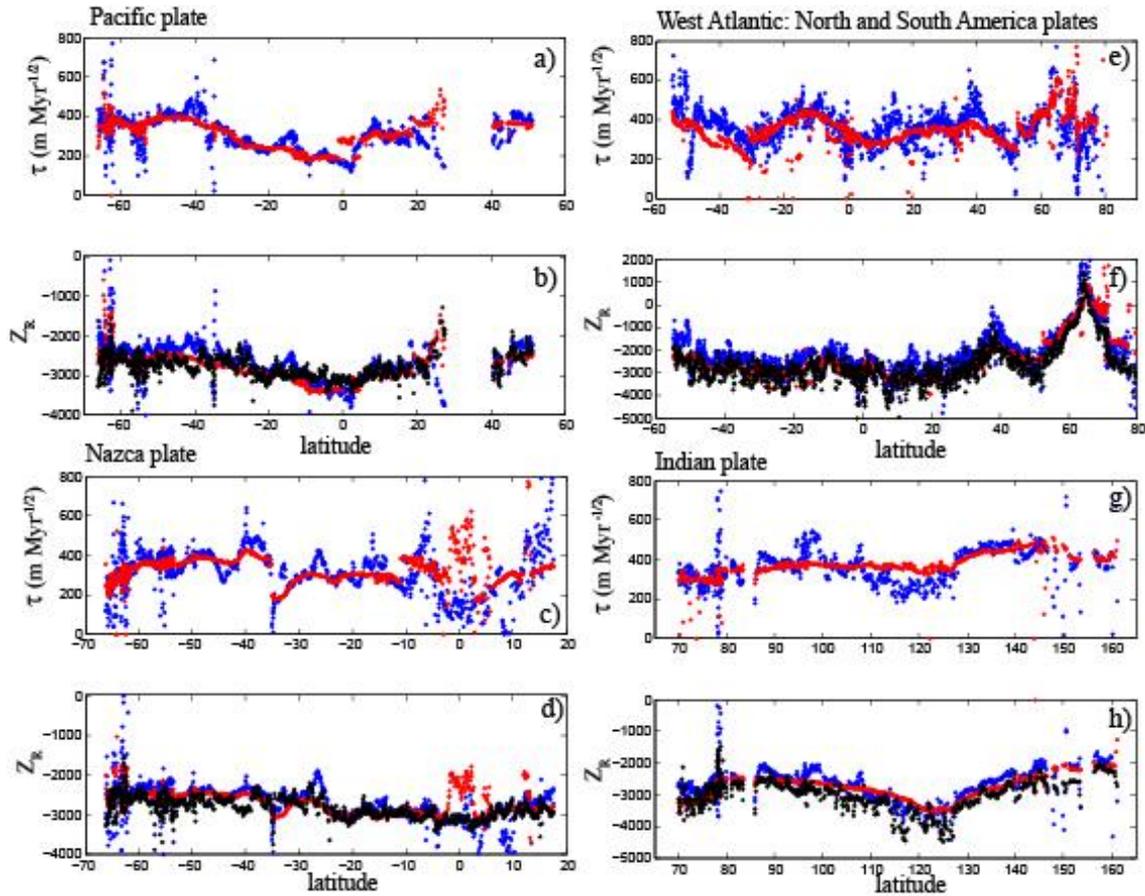
Figure 3

Figure 4

Figure 5

a)

b)

bathymetry/topography (m)

c)

d)
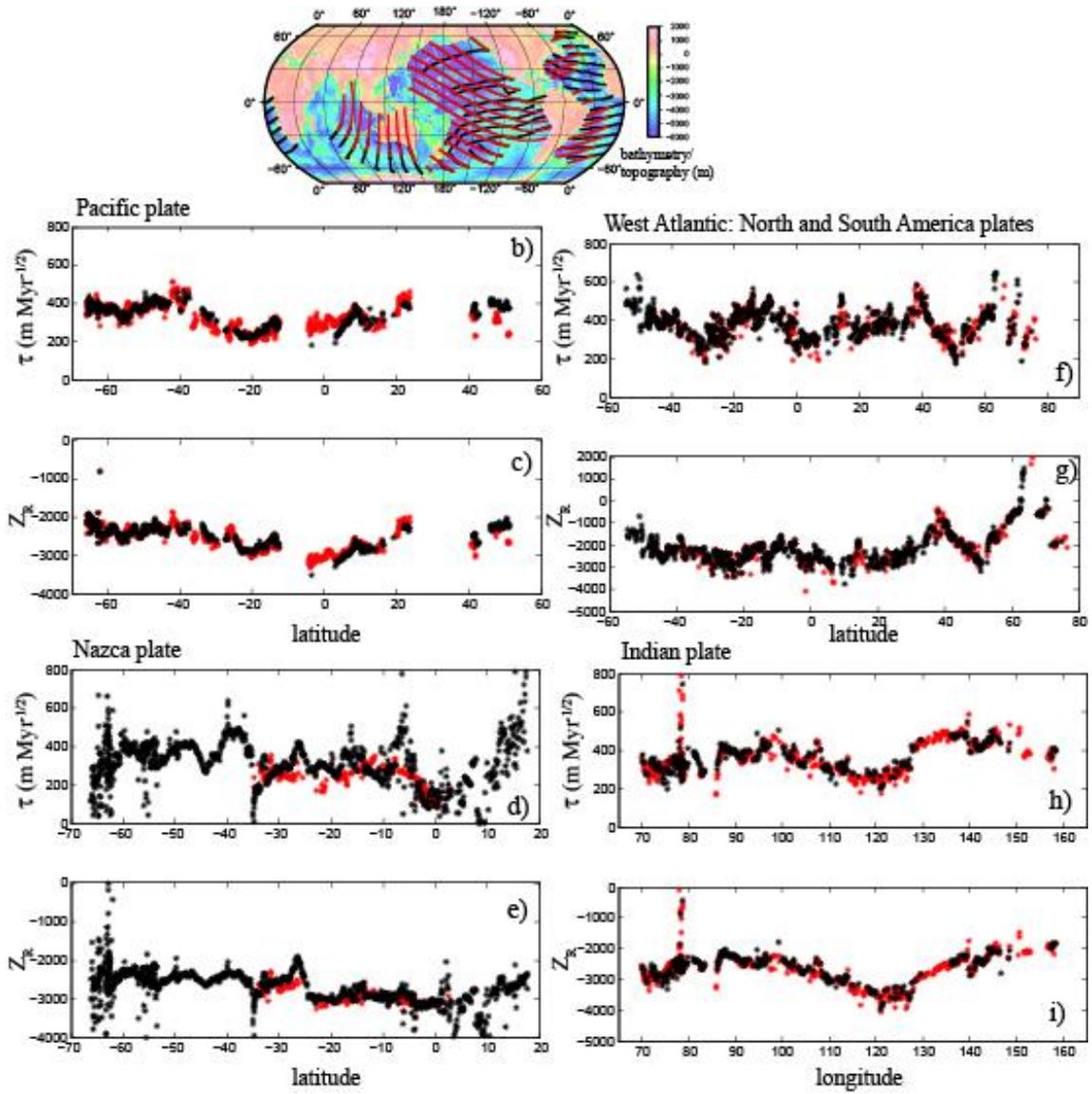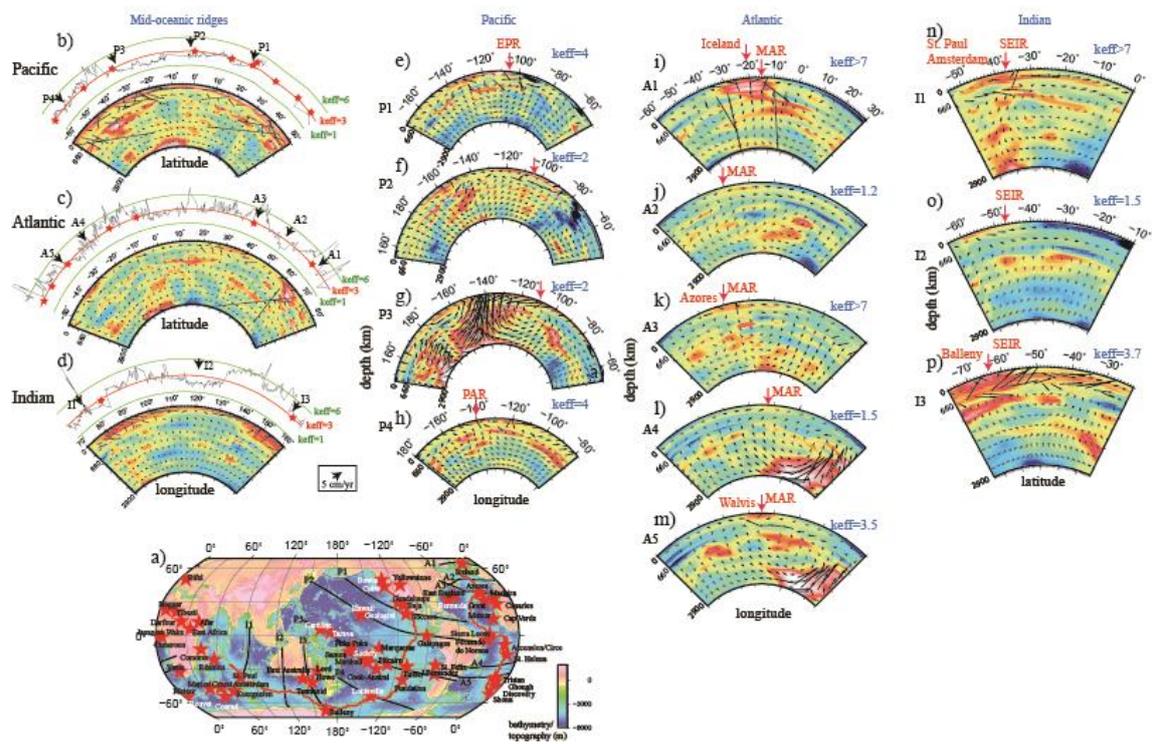
Figure 6

Figure 7

Figure 8

Figure 9